Contrib Mineral Petrol (2006) 152:523–540
DOI 10.1007/s00410-006-0121-4

ORIGINAL PAPER

Rhyodacite magma storage conditions prior to the 3430 yBP caldera-forming eruption of Aniakchak volcano, Alaska

Jessica F. Larsen

Received: 20 December 2005 / Accepted: 31 May 2006 / Published online: 26 July 2006
© Springer-Verlag 2006

Abstract This study presents a pre-eruptive magma storage model for the rhyodacite and andesite magmas erupted during the 3430 yBP caldera-forming eruption of Aniakchak volcano, Alaska, derived from phase equilibria experiments and petrological data. The compositions of Fe–Ti oxide pairs from the early erupted Plinian rhyodacite pumice yield core temperatures of 871–900°C, with rims up to ~942°C, and fO_2 from –10.6 to –11.8 log units. Melt inclusions entrapped in plagioclase phenocrysts have H_2O contents between 3 and 5 wt%, estimated by FTIR and electron microprobe volatiles by difference methods, with no detectable CO_2. Assuming water saturation, this corresponds to entrapment pressures between ~65 and 150 MPa. Phase equilibria results reproduce the natural phase assemblages at P_{H_2O} of 95–150 MPa at 870–880°C, assuming water saturation. A mismatch in experimental versus natural glass SiO_2 and Al_2O_3, and MELTS models for H_2O-undersaturated conditions indicate that the rhyodacite may not have been H_2O saturated. MELTS models with $X_{H_2O} = 0.8$ and P_{total} of 125–150 MPa at 870–880°C reproduce the natural groundmass glass Al_2O_3 composition best, indicating the magma may have been slightly H_2O undersaturated. Those pressures correspond to storage at 4.5–5.4 km depth in the crust. MELTS models and VBD estimates from melt inclusions in titanomagnetite grains from the andesite indicate pre-eruptive conditions of ~1,000°C and > 110 MPa, corresponding to a minimum residence depth of ~4.1 km assuming water saturation or greater if the magma was H_2O undersaturated. Previous geochemical studies indicate separate histories of the two magmas, though they retain some evidence that they are ultimately related through fractional crystallization processes. Analogous to the 1912 Novarupta magmas, the rhyodacite and andesite presumably originated within the same crystal mush zone beneath the edifice, yet were separated laterally and underwent different degrees of crustal assimilation. The andesite must have resided in close proximity, with ascent occurring in response to movement of the rhyodacite, and resulting in extensive syn-eruptive mingling.

Communicated by T.L. Grove

Electronic Supplementary Material Supplementary material is available for this article at http://dx.doi.org/10.1007/s00410-006-0121-4 and is accessible for authorized users.

J. F. Larsen (✉)
Alaska Volcano Observatory, Geophysical Institute,
University of Alaska, Fairbanks, AK 99775, USA
e-mail: faust@gi.alaska.edu

Introduction

Large volume, caldera-forming eruptions (CFEs) present significant proximal hazards and could trigger short-term global climate change. Petrology studies providing constraints on pre-eruptive magma storage and movement lead to a better understanding of the causes of these spectacular events. Aniakchak caldera is located 670 km southwest of Anchorage on the Alaska Peninsula (Fig. 1). The caldera is 10 km in diameter and was created during the 3430 ^{14}C yBP CFE (Miller and Smith 1977, 1987). This event produced voluminous and highly mobile rhyodacite and andesite pyroclastic flow deposits (Miller and Smith

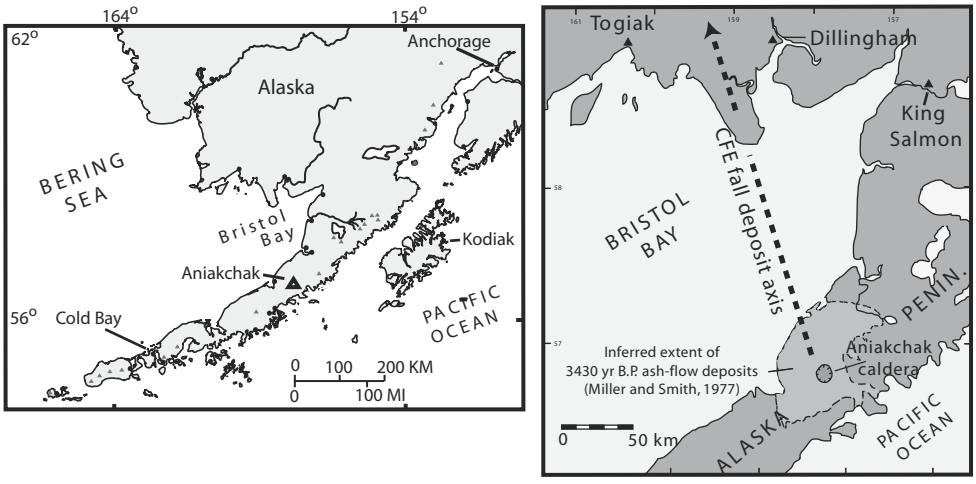

Fig. 1 **a** Location map of the Alaska Peninsula and Aniakchak volcano. **b** Regional map showing the approximate extent of the CFE ash flow sheet. The *dashed line* illustrates the axis along which the Plinian phase deposits are thickest. After Waythomas and Neal (1998) and Neal et al. (2001)

1987; Dreher et al. 2005) and is thought to have contributed to a period of global climate cooling (Miller and Smith 1987; Begèt et al. 1992). This eruption has been the focus of general investigations on calderas in the Aleutian arc (Miller and Smith 1977, 1987), geologic investigations by the Alaska Volcano Observatory (e.g., Waythomas et al. 1996; Waythomas and Neal 1998; Neal et al. 2001), and geochemistry, petrology, and physical volcanological studies (Dreher 2002; George et al. 2004; Dreher et al. 2005). It produced a minimum of 14 km^3 dense rock equivalent (DRE) calc-alkaline rhyodacite (68–70 wt% SiO_2) and 13 km^3 DRE andesite (58–60 wt% SiO_2; Dreher 2002; Fig. 2). The eruption deposits comprise early rhyodacite Plinian pumice fall, a middle section of mingled rhyodacite and andesite pyroclastic flow, and late-erupted andesite pyroclastic flow deposits (Fig. 1). Significant banding is present in pumice clasts from the mingled rhyodacite/andesite portion of the pyroclastic flow sheet. This banding has been observed to persist on the 10's of microns scale in scoria clasts from the late erupted, ''purely'' andesite pyroclastic flow deposits. No obvious banding is observed in the Plinian rhyodacite pumice fall deposits that erupted first (Dreher 2002).

Geochemical models of the Aniakchak CFE deposits derived from Sr, Nd, and U isotopic data (George et al. 2004) are used by Dreher et al. (2005) to infer magmatic relationships prior to the eruption. The results of their study indicate that the rhyodacite and andesite may not be related simply through fractionation, and crustal contamination and hybridization may play an important role in production of the andesite in particular. Their models are interpreted to reflect complex mixing with magma remaining from a batch that produced a precaldera rhyodacite fall deposit exposed along the caldera rim. Dreher et al. (2005) use the geochemical data to interpret the rhyodacite as having originated deep within the crust, intersecting a shallow, hybrid andesite magma chamber prior to eruption.

The goal of this study is to use high pressure and temperature experiments and petrological data from the eruptive products to provide a model of the pre-eruptive magma storage and dynamics of the 3430 yBP Aniakchak magmas, focusing primarily on the rhyodacite. The CFE rocks are crystal-poor and the groundmass glass compositions show only small degrees of evolution away from the bulk rocks. This makes the phase equilibria approach difficult to apply to the nearly aphyric CFE andesite, and its storage conditions are estimated here using a combination of MELTS modeling and melt inclusion volatile concentrations. The Aniakchak rhyodacite contains equilibrium Fe–Ti oxide pairs suitable for geothermometry, and melt inclusions in plagioclase provide initial estimates on crystallization depths through H_2O contents. The petrological data provide independent constraints that can be compared with the phase equilibria experimental results to provide a model of the pre-eruptive history of the rhyodacite magma. The model resulting from the experimental work is compared with the magma storage and genetic models discussed by Dreher et al. (2005).

Methods

Experimental techniques

Sample 98ACJL1B collected from Plinian fall deposits along the Bering coast (Fig. 1) provided the experimental starting material, because the pumices are early erupted and are the samples used in the petrological

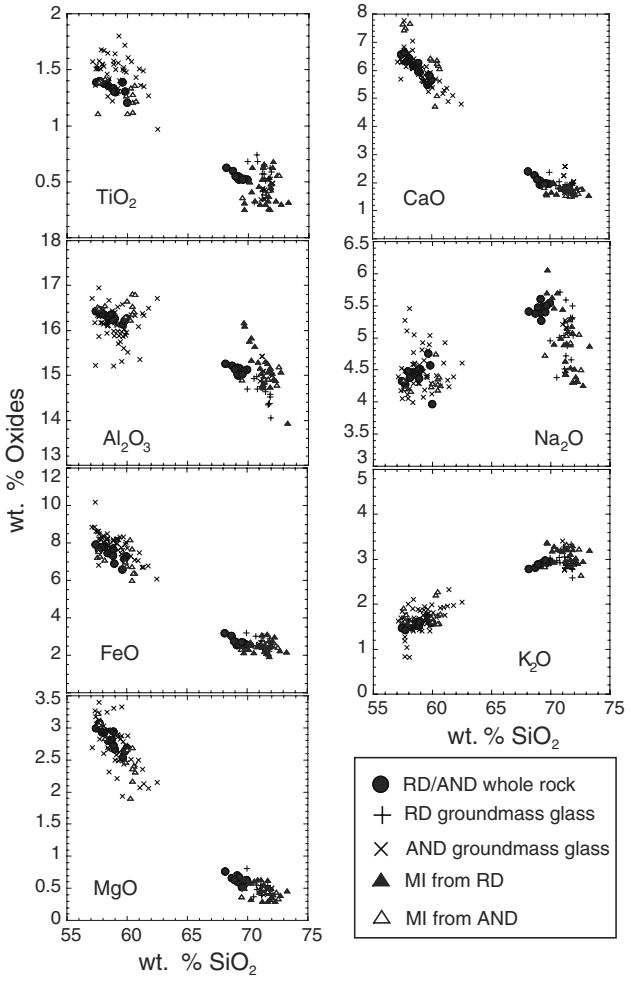

Fig. 2 Harker diagrams plotting major oxide compositions of the whole rock juvenile rhyodacite (RD) pumice and andesite (AND) scoria, groundmass glass, and melt inclusions against wt% SiO_2. Whole rock XRF analyses are those reported in Dreher (2002), and shown in Fig. 6 of Dreher et al. (2005). *MI* denotes melt inclusion analyses. All glass analyses shown in this figure were collected for this study (electronic supplement) separate from Dreher (2002) and Dreher et al. (2005). The melt inclusions from plagioclase phenocrysts from the andesite have rhyodacitic compositions and overlap those analyzed from plagioclase found in the rhyodacite. This provides evidence for crystal exchange between the rhyodacite and andesite magmas prior to or during the eruption

portion of the study. The experimental methods used for the phase equilibria runs are similar to those reported in Hammer et al. (2002) and Larsen (2005). Preparation of the starting powders involved cleaning the pumice clasts ultrasonically in de-ionized water and hand crushing them under ethanol using ceramic and agate mortar and pestle. The crushed powders were loaded into 5 mm OD $Ag_{70}Pd_{30}$ or Au tubes, with ~20 wt% de-ionized water to ensure vapor saturation, and sealed into the capsule by welding. Experiments run below ~900°C and 200 MPa utilized Waspaloy® cold seal pressure vessels buffered at fO_2 of Ni–NiO + 0.5 to 1 log unit (NNO + 0.5 to 1) by using a Ni filler rod. The experiments run in Au served to check the phase assemblages in case of Ni infiltration. Cpx, possibly stabilized by Ni, crystallized in ACP8 but failed to form in repeat experiment ACP10, run in Au tubing. Temperatures above ~900°C required a titanium–molybdenum–zirconium (TZM) alloy pressure vessel enclosed in an Inconel sheath, and bathed in argon gas. Those sample assemblies consisted of an outer $Ag_{70}Pd_{30}$ sample tube, ~20 wt% de-ionized water, and a separate Pt capsule filled with Ni metal foil and NiO powder. This buffer assembly served to monitor capsule fO_2, which was fixed through fH_2 by adding 2–3 bar of CH_4 gas to the ultra-high purity Ar pressurizing gas. The quench process involved dropping the TZM vessel rapidly into a bucket of cold water upon removal from the furnace. Reversal experiments were conducted by running glass- and crystal-rich experimental materials simultaneously at an intermediate *P* and *T* condition, to help verify the position of the phase stability curves.

Analytical techniques

The whole rock geochemical data derived from Dreher (2002) came from the Washington State University Geoanalytical Lab and a detailed description of the methods and analytical precision and accuracy can be found in Johnson et al. (1999). Quantitative analyses of mineral phases in the experimental and natural samples were conducted using a 15 KeV, 10 nA, and a focused (~1 μm) beam using the Cameca SX-50 electron microprobe in the Advanced Instrumentation Laboratory at the University of Alaska, Fairbanks (UAF). The nearly aphyric natural samples have some mineral phases that are present in very small amounts. Probe data from pyroxenes and amphiboles were conducted using grain mounts from crystal concentrates. Mineral phases crystallizing in the experiments are typically a few to 10's of μm across, and some were too small to analyze. During each microprobe session, a 30 KeV, 20 nA scanning beam was used to help locate the mineral phases of interest in each sample through the difference in brightness in the backscattered electron image (BSE). Each crystal targeted for analysis was first confirmed using the EDAX energy dispersive spectrometer (EDS).

All hydrous and nominally anhydrous natural and experimental glasses were analyzed using operating conditions of 15 KeV, 10 nA, and a defocused (~10 μm) beam to minimize Na migration (e.g. Devine et al. 1995). Accurate Na compositions required

collecting Na counts first, and measuring the decay in Na counts with time over 16 s. A linear fit to the Na decay data was used to correct the decreasing Na counts back to the original, and most accurate values collected early in the analyses. This procedure was conducted using a self-calibrating correction routine within the Probe for Windows© software package used at UAF. Since hydrous silicate glasses can be problematic, the standardization routine also included 5–7 data points collected on polished chips from the set of hydrous glasses studied by Devine et al. (1995). The VBD method was used to estimate the amount of water in each hydrous glass standard, and checked against the published compositions prior to each microprobe session. Rhyolite glass standard KN18 was analyzed before, after, and often during each microprobe session when the unknown samples were changed. The KN18 analyses were ratioed with their published values (Devine et al. 1995) to be used to normalize the SiO_2, Al_2O_3, Na_2O, K_2O, and total FeO compositions of the unknown glasses. CaO data in the experimental glasses tended to be systematically low by ~0.25 wt%. Glasses synthesized at super liquidus conditions were checked against the bulk compositions and used to apply an additional correction to CaO in all experimental glass runs.

Melt inclusion analyses

Melt inclusions in plagioclase phenocrysts were prepared for Fourier transform infrared spectroscopy (FTIR) measurements. Although plagioclase is usually suspected of leaking (e.g., Tait 1992), the largest and most abundant inclusions in the Aniakchak rhyodacite reside within plagioclase. Pyroxenes and amphibole also contain melt inclusions but they are too small (<30 μm) to analyze using FTIR. Plagioclase phenocrysts from fresh pumice clasts from the Bering coast outcrop were picked after washing the glass away gently using a shallow watch glass and submerging each in mineral oil to find suitable melt inclusions (i.e. one shrinkage bubble and no visible cracks). Those crystals were mounted on a glass slide using acetone soluble Crystal bond 509 and doubly polished to expose the chosen melt inclusions on both sides.

The FTIR analyses were conducted at the USGS in Menlo Park using a Nicolet Magna 750 spectrometer coupled with an IR microscope and LN-cooled MCT detector. Each inclusion was centered on a 100-μm pinhole, and two adjustable, square apertures were used to select the region bounded only by the exposed inclusion for analyses. Each spectra contained H_2O absorbance peaks, but no detectible CO_2. The heights of the 4,500 and 5,200 cm^{-1} absorption peaks were used to calculate H_2O contents through the Beer–Lambert relationship, using ε 1.50 and 1.86 l mol^{-1} cm^{-1} for 4,500 and 5,200 cm^{-1} vibrations, respectively (Ihinger et al. 1994), and melt density of 2,300 kg/m^3. Thicknesses were estimated using a spindle stage and pin gauge and contribute the greatest source of error to the water concentrations.

Results

Rhyodacite and andesite natural phase assemblages

The Aniakchak rhyodacite from both Plinian and ash-flow deposits is crystal-poor, containing ~9 vol% phenocrysts of plagioclase, hypersthene, augite, magnetite, ilmenite, and amphibole. The equilibrium phase assemblage consists of all those phases, except augite, which is rare and suspected of being a xenocryst, as discussed below. Using the phase compositions listed in Tables 1, 2, and 3, a linear least squares mass balance provides estimates of the proportion of each phase. The proportions are 93–94 vol% glass, 5.4–6.4 vol% plagioclase, 0.53–0.57 vol% hypersthene, 0.26–0.28 vol% amphibole, and 0.01–0.03 vol% magnetite, with rms error of 0.016–0.022. The ranges represent models fit using a range of plagioclase compositions, from An_{33} to An_{40}.

The Aniakchak andesite is also crystal-poor, containing a similar proportion of phenocrysts as the rhyodacite, by weight. The andesite contains plagioclase, hypersthene, augite, magnetite, and rare olivine and quartz (Dreher et al. 2005). The olivine and quartz indicate that the andesite has a heterogeneous and disequilibrium phenocryst assemblage, arising from crustal assimiliation or magma mixing (Dreher et al. 2005). Evidence for crystal exchange between the CFE rhyodacite and andesite exists primarily in plagioclase and pyroxenes. This accompanies the macroscopic evidence for mingling found in ash flow deposits that contain unmingled rhyodacite and andesite, along with banded pumice.

Glasses

The rhyodacite groundmass glass and melt inclusion major oxide data are presented in Table 1, Fig. 2 and the electronic supplement. The rhyodacite groundmass glass is microlite free, with 69–72 wt% SiO_2 (Fig. 2). However, the groundmass glass analyses are fairly scattered in most of the major oxides (Fig. 2), reflecting local variability on the approximate scale

Table 1 Representative major element compositions of the bulk starting materials

Oxide	RD bulk[a]	AND bulk[a]	RD MG	AND MG	RD MI
SiO_2	70.57	58.7 (8)[b]	71.5 (4)	58.6 (8)	71.3 (9)
TiO_2	0.53	1.34 (05)	0.54 (02)	1.47 (13)	0.43 (14)
Al_2O_3	15.31	16.3 (01)	14.48 (20)	16.11 (38)	15.17 (47)
FeO_t	2.69	7.43 (38)	2.60 (14)	8.10 (54)	2.46 (32)
MnO	0.16	0.20 (01)	–	–	–
MgO	0.61	2.82 (17)	0.50 (04)	2.83 (32)	0.47 (11)
CaO	2.00	6.13 (36)	1.91 (04)	6.11 (49)	1.73 (13)
Na_2O	5.38	4.42 (19)	5.22 (05)	4.51 (34)	4.98 (49)
K_2O	2.97	1.57 (07)	2.96 (16)	1.61 (29)	3.12 (16)
P_2O_5	0.11	0.56 (05)	0.08 (04)	–	–
Cl	–	–	0.20 (10)	0.11 (02)	–
Total[c]	99.60	99.85	99.80	99.27	96.01
n[d]	1	35	9	43	25

RD rhyodacite, *AND* andesite

[a]XRF analysis of major oxides in the RD collected by the WSU Geoanalytical Lab have an estimated accuracy within 1% for all elements reported (Johnson et al. 1999). The AND bulk composition estimated from electron microprobe analyses on a fused glass bead, prepared and analyzed at UAF

[b]Numbers in parentheses represent the standard deviation of n analyses

[c]Analyses normalized to 100% volatile-free, with the original totals included

[d] n, number analyses. In the case of RD bulk, XRF analyses were conducted on two splits from powders crushed from a single pumice block

(or larger) of the microprobe beam. In particular, Al_2O_3 and Na_2O compositions appear to be the most affected, with values extending ~1 wt% below the average contents of the bulk pumice. This could signify depletion of Na and Al from the melt in response to plagioclase crystallization in the magma.

The CFE andesite glass compositions are presented in Table 1, Fig. 2 and the electronic supplement. The andesite glass data tend to span a wider range in SiO_2 (~57 to >70 wt%) than the rhyodacite because of pervasive banding on both the macro (cm) and/or micro (μm) scale in all CFE andesite clasts studied. In the middle of the stratigraphic section where mingling is most pronounced, the pumices are clearly banded, and thin sections of those samples reveal major oxide glass compositions that extend partway through the compositional gap outlined by the bulk rock compositions from the separate rhyodacite and andesite deposits (Fig. 2). Isolated regions of clear, rhyodacite glass on a 10-μm spatial scale also exist in scoria samples from the upper, andesite-dominant ash flow deposits and groundmass glass data from those scoria clasts also show variability in SiO_2 based on the fine-scale banding (Fig. 3). It is important to note, however, that the compositional trends in the andesite groundmass glass data do not extend completely through the gap in SiO_2 outlined prominently by the whole juvenile clast data set. This shows that although mingling was pervasive throughout the eruption, hybridization between the two magmas probably occurred only to a very limited extent.

The melt inclusions from plagioclase in the rhyodacite are found in the cores of ~1 mm An_{39} plagioclase phenocrysts, and are compositionally similar to the groundmass glass (Table 1). The melt inclusion Al_2O_3 diverges the most among the oxides from the bulk pumice values, with Na_2O showing a similar depletion as the groundmass glass. The Al_2O_3 data are scattered, with one point showing ~1 wt% depletion relative to the bulk data, but most data extending up to ~1 wt% greater contents than the bulk and ~2 wt% greater than the most depleted groundmass glass. If the melt inclusions reflect entrapment of the melt existing with the magma at its last storage conditions, it is expected that Al_2O_3 would also show ~1 wt% depletion relative to the bulk pumice data, as seen in the groundmass glass analyses. It is possible that some of those analyses resulted from overlap between the microprobe beam and the adjacent plagioclase crystal. If this was always the case, however, there should be a concurrent increase in Na in the same analyses, but only one data point shows elevated Na as well.

Melt inclusion major oxide analyses from magnetite and plagioclase phenocrysts in the andesite are also shown in Fig. 2. Inclusions derived from plagioclase crystals are all rhyodacite, while those analyzed within magnetite are andesite (Fig. 2, electronic supplement). Also, some of the andesite composition inclusions

Table 2 Representative rhyodacite and andesite phenocryst compositions

Oxide	RD Amph	RD Opx	RD Cpx	AND Opx	AND Cpx[a]
SiO_2	43.5 (3)	53.1 (8)	51.9 (3)	52.3 (3)	51.7 (5)
TiO_2	3.82 (24)	0.24 (03)	0.44 (10)	0.25 (11)	0.74 (10)
Al_2O_3	11.3 (1)	0.7 (1)	1.5 (3)	0.6 (1)	2.9 (4)
FeO_t	12.19 (32)	20.20 (88)	11.21 (46)	20.08 (1.36)	8.25 (32)
MnO	0.47 (08)	0.44 (03)	0.25 (02)	1.32 (60)	0.26 (09)
MgO	14.66 (19)	22.38 (44)	14.19 (29)	22.47 (60)	15.23 (20)
CaO	11.35 (22)	1.41 (14)	19.57 (43)	1.58 (45)	20.94 (54)
Na_2O	2.54 (07)	0.03 (02)	0.36 (01)	0.03 (01)	0.30 (03)
K_2O	0.49 (03)	–	–	–	–
Cl	0.05	–	–	–	–
F	0.31	–	–	–	–
Total	100.84	98.49	99.45	98.59	100.35
n[b]	10	19	6	3	8
Mol%[c]	–	3–64–33	41–41–19	3–63–34	43–43–13

Oxide	RD Pl[a]	AND Pl1[a]	AND Pl2[a]	AND Pl3[a]
SiO_2	58.5 (1.6)[d]	58.4 (1.0)[d]	54.1 (6)	47.2 (1.0)
TiO_2	–	–	–	–
Al_2O_3	26.3 (1.0)	25.94 (7)	28.6 (6)	32.9 (1.1)
FeO_t	0.43 (13)	0.41 (10)	0.60 (12)	0.80 (19)
MnO	–	–	–	–
MgO	–	–	–	–
CaO	8.2 (1.2)	8.16 (68)	11.66 (56)	17.00 (92)
Na_2O	6.81 (12)	7.02 (39)	5.06 (26)	2.01 (50)
K_2O	0.34 (11)	0.29 (04)	0.15 (04)	0.04 (02)
Total	100.67	100.25	100.17	99.87
n[b]	45	44	16	15
Mol%[c]	39	30–40	52–59	78–88

Mineral phases are labeled as follows: *Pl* plagioclase, *Cpx* augite, *Opx* hypersthene, *Ol* olivine, *Amph* amphibole

[a]Average analyses of plagioclase reported after Dreher (2002) and Dreher et al. (2005) are included here for reference. The original data is published in Dreher (2002) PhD thesis, and histograms of the data are presented in Dreher et al. (2005). Opx, Cpx, and Amph analyses were conducted for this study

[b]n, number of individual crystals analyzed in each sample

[c]Mol% refers to the average anorthite component in the plagioclase and Wo–En–Fs in pyroxene

[d]The numbers in parentheses represent 1σ about the average of n individual analyses and are larger than the individual analytical errors on each data point

found in magnetite are slightly enriched in SiO_2. The compositional deviations from the groundmass glass values may reflect variable inward crystallization in the melt inclusions contained in both magnetite and plagioclase.

Plagioclase

Figure 4 in Dreher et al. (2005) shows histograms of plagioclase analyses for both CFE rhyodacite and andesite. Those data are derived from analyses published as an appendix in his PhD thesis (Dreher 2002), and are limited in number and undifferentiated with respect to crystal size, shape, texture, and the position of the microprobe beam. Average plagioclase compositions from Dreher (2002) are given in Table 2, since the compositional analyses are only available as an appendix to the thesis. Additional analyses were also collected for this study (Table 2) primarily to ascertain whether the phenocryst modal compositions shown in the histogram of Dreher et al. (2005) correspond to plagioclase confined to distinct size ranges or textures.

The data published in Dreher et al. (2005) show plagioclase compositions of ~$An_{30–53}$ from the rhyodacite. Data below An_{30} shown in Fig. 4 of Dreher et al. (2005) should be disregarded, since the low An analyses published in Dreher (2002) show significantly elevated SiO_2 and reduced Al_2O_3 consistent with beam overlap with adjoining glass. The additional analyses collected here from plagioclase from Plinian fall and ash flow rhyodacite pumice samples are compositionally similar, ranging between An_{33} and An_{41} (Table 2). Although most plagioclase in the rhyodacite are euhedral and prismatic, including those analyzed for

Table 3 Rhyodacite Fe–Ti oxide pair compositions

Pair	T1c[a,b]	T2	T3	T4r	P2r[b–d]	P2c
Titanomagnetite						
TiO_2	11.29	11.62	11.55	11.69	11.59 (28)	11.95 (24)
Al_2O_3	2.26	2.15	2.21	2.16	2.25 (08)	2.29 (01)
FeO_t	78.33	80.21	80.30	78.97	77.82 (2.51)	78.95 (20)
MnO	1.18	1.33	1.16	1.25	1.23 (14)	1.24 (03)
MgO	1.94	1.99	2.02	2.12	2.12 (15)	2.03 (10)
Cr_2O_3	0	0.05	0.02	0.01	0	0
Total	95.00	97.37	97.26	96.19	95.01	96.46
Ilmenite						
TiO_2	44.17	44.03	42.95	41.17	43.68 (75)	39.7 (1.5)
Al_2O_3	0.20	0.21	0.22	0.45	0.27 (04)	0.43 (05)
FeO_t	48.40	48.70	48.17	51.87	50.02 (22)	51.99 (17)
MnO	1.52	1.71	1.48	1.44	1.43 (05)	1.60 (07)
MgO	3.41	3.42	3.43	3.02	3.36 (02)	3.32 (11)
Cr_2O_3	0	0	0	0	0.02 (02)	0.02 (02)
Total	97.71	98.08	96.25	97.95	98.77	97.05
Temperature[e]	883 (20)	888 (21)	891 (21)	923 (20)	942 (21)	901 (21)
fO_2	– 11.44	– 11.32	– 11.24	– 10.55	– 10.18	– 11.07

Pair	P4r	P4c	P5r	P5c	P6r	P6c
Titanomagnetite						
TiO_2	11.68 (11)	12.14 (14)	11.98 (10)	12.41 (24)	11.97 (39)	11.90 (18)
Al_2O_3	2.19 (02)	2.17 (08)	2.11 (06)	2.07 (03)	2.13 (08)	2.21 (08)
FeO_t	79.96 (41)	79.60 (70)	79.08 (54)	79.21 (38)	79.15 (97)	79.65 (63)
MnO	1.24 (11)	1.29 (11)	1.22 (08)	1.18 (05)	1.21 (12)	1.28 (12)
MgO	2.03 (07)	2.07 (05)	2.03 (02)	2.02 (10)	2.11 (08)	2.06 (11)
Cr_2O_3	0.01 (01)	0.01 (01)	0.02 (02)	0.02 (02)	0.01 (01)	0.03 (02)
Total	97.09	97.28	96.4	96.9	96.58	97.13
Ilmenite						
TiO_2	43.44 (34)	43.69 (26)	45.96 (36)	44.81 (66)	45.53 (21)	44.9 (1.2)
Al_2O_3	0.26 (01)	0.23 (01)	0.23 (04)	0.24 (03)	0.22 (01)	0.24 (02)
FeO_t	48.71 (26)	49.01 (79)	48.58 (63)	48.70 (31)	48.41 (18)	48.23 (65)
MnO	1.56 (11)	1.49 (02)	1.53 (14)	1.51 (01)	1.52 (12)	1.59 (18)
MgO	3.28 (08)	3.24 (06)	3.24 (07)	3.30 (16)	3.29 (05)	3.37 (06)
Cr_2O_3	0.02 (02)	0.01 (01)	0.02 (02)	0.03 (01)	0	0.01 (01)
Total	97.26	97.69	99.55	98.60	98.97	98.34
Temperature[e]	899 (21)	892 (21)	895 (22)	875 (23)	882 (22)	878 (22)
fO_2	– 11.17	– 11.25	– 11.34	– 11.75	– 11.55	– 11.67

Pair	P7r	P7c	P9r	P9c	P11a
Titanomagntite					
TiO_2	12.21 (08)	12.34 (28)	12.15 (18)	12.43 (07)	14.381 (11)
Al_2O_3	2.11 (08)	2.15 (07)	2.15 (10)	1.95 (03)	0.90 (02)
FeO_t	79.78 (47)	79.00 (71)	79.24 (35)	79.24 (35)	74.64 (42)
MnO	1.24 (03)	1.23 (06)	1.35 (08)	1.22 (05)	1.06 (11)
MgO	2.09 (09)	2.01 (07)	1.96 (04)	1.94 (03)	1.77 (03)
Cr_2O_3	0.02 (02)	0.01 (01)	0.01 (01)	0.01 (01)	0.02 (02)
Total	97.45	96.75	96.87	96.88	92.78
Ilmenite					
TiO_2	45.14 (99)	45.70 (59)	45.29 (19)	45.10 (41)	43.63 (53)
Al_2O_3	0.26 (03)	0.21 (02)	0.23 (02)	0.22 (03)	0.10 (01)
FeO_t	49.02 (06)	48.82 (43)	48.98 (19)	48.9 (30)	48.87 (61)
MnO	1.55 (03)	1.58 (06)	1.41 (24)	1.56 (12)	1.29 (08)
MgO	3.18 (04)	3.25 (02)	3.17 (01)	3.18 (02)	2.64 (01)
Cr_2O_3	0.02 (02)	0.04 (04)	0.01 (01)	0.02 (02)	0.05 (05)
Total	99.16	99.38	99.10	99.04	94.57

Table 3 continued

Pair	P7r	P7c	P9r	P9c	P11a
Temperature	889 (22)	887 (22)	893 (22)	871 (21)	931 (25)
fO_2	– 11.48	– 11.46	– 11.39	– 11.53	– 10.98

[a]T1c, T2, T3, and T4 denote core to rim transect analyses, with c denoting core and r denoting rim. T2 and T3 are transitional between the core and rim

[b]Typical analytical errors on single analysis are similar to those reported in Izbekov et al. (2004), using the same analytical routine in Probe for Windows

[c]P-pair number, r-rim, c-core, a-average

[d]Except for the transect points T1–4, each reported analysis is the average of three electron microprobe data points. The numbers in parentheses represent the standard deviation about the mean of the average value reported

[e]All pairs reported in this table pass the MgO/MnO equilibrium criteria of Bacon and Hirschmann (1988)

this study, a few plagioclase grains have embayed edges and dissolution features aligned along cleavage planes parallel to the longest axis of the crystals.

The plagioclase phenocrysts in the andesite appear to comprise three distinct populations, based upon core compositions presented in Dreher et al. (2005), with an overall range from ~$An_{30–88}$. The andesite populations are approximately divided into three modes: $An_{30–40}$, $An_{52–59}$, and $An_{78–88}$. For the present study, additional microprobe work was conducted specifically to verify the sizes and textures of the crystals producing the different modes. The $An_{78–88}$ crystals are coarsely sieved. Several $An_{30–40}$ plagioclases are found embedded in regions of clear, rhyodacite glass. The $An_{52–59}$ grains tend to be unsieved elongate and tabular phenocrysts and microphenocrysts (Fig. 3). The links between the different textures and the compositional modes lend additional support for heterogeneous plagioclase populations in the andesite. The lower An plagioclase embedded in clear, rhyodacite glass indicates crystal exchange between the two CFE magmas occurred prior to or during the eruption, perhaps coincident with the mingling that produced the bimodal ash flow deposits and banded pumice.

Pyroxenes and amphibole

Both Aniakchak rhyodacite and andesite contain ortho and clinopyroxenes and the compositions of those phases presented here result from microprobe work

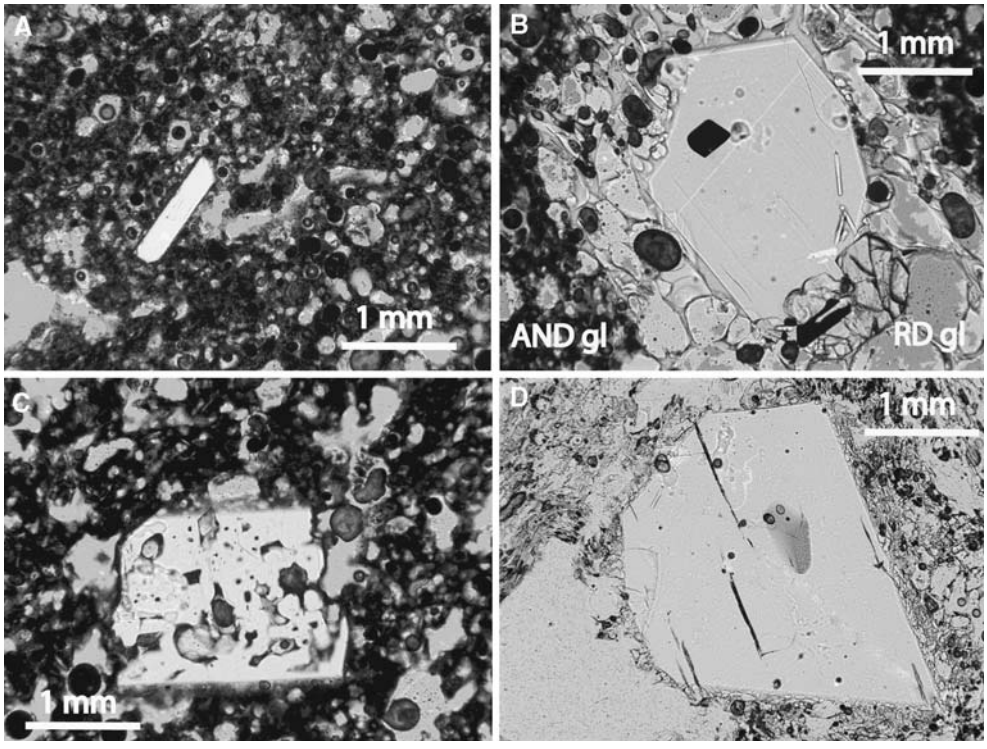

Fig. 3 Photomicrographs of plagioclase from Aniakchak CFE rhyodacite and andesite samples. **a** Representative plagioclase phenocryst from ACAF1D1 andesite scoria sample (Dreher 2002). This plagioclase is typical of those with $An_{52–59}$ compositions. **b** Representative plagioclase phenocryst (~$An_{30–40}$) typically found within rhyodacitic glass (RD gl), embedded in andesite glass (AND gl) in scoria from location ACAF1E5 (Dreher 2002). **c** Coarsely sieved plagioclase crystal representative of those with ~$An_{78–88}$ compositions from scoria from ACAF1E5 location. **d** Euhedral plagioclase from Plinian fall section AC36a (same location as 98ACJL1B), representative of those with $An_{30–40}$ compositions

conducted specifically for this study (Table 2). The rhyodacite pyroxenes have compositions of $Wo_{3–4}$, $En_{60–64}$, $Fs_{32–36}$ and $Wo_{41–42}$, $En_{41–42}$, $Fs_{17–19}$, classifying them as hypersthene and augite (Table 2). Both types of pyroxenes are unzoned and euhedral to slightly rounded. Augite is very rare in the rhyodacite, and is found only after crystal concentrates of the crushed pumice are examined for mafic phases. Its scarcity indicates that it is xenocrystic, and may have originated within the co-erupted andesite. The amphiboles are classified as pargasitic hornblende (Table 2), and do not have reaction rims. The amphibole also tends to be rare, yet is present in greater abundance than the augite.

The hypersthene and augite pyroxenes found within the andesite have average compositions of $Wo_3En_{63}Fs_{34}$ and $Wo_{43}En_{43}Fs_{13}$, both unzoned, and euhedral or subrounded. The hypersthenes from the andesite overlap in composition with those from the rhyodacite. Hypersthene is very rare in the andesite and some are found within regions of clear rhyodacite glass, as described for the $An_{30–40}$ plagioclase also found within the andesite. It is possible that the hypersthenes are xenocrystic, and originated through crystal exchange with the co-erupted rhyodacite during syn-eruptive mingling. Augite found in the andesite is slightly more calcic than those in the rhyodacite, although the compositions of the two groups are very similar (Table 2).

Constraints on temperatures and fO_2 from the natural samples

Samples from the Plinian phase rhyodacite pumice contain magnetite and ilmenite, with some unexsolved, euhedral touching pairs suitable for estimating pre-eruptive magmatic temperatures. Temperatures and oxygen fugacities (fO_2) were estimated from the pair compositions using the model of Andersen and Lindsley (1988), and the mineral reformulation model of Stormer (1983), with all compositional and model data presented in Table 3. The first four sets of data listed in Table 3 represent single points in a traverse across one of the oxide pairs studied. The other analyses are separated into averages of the analyses from core and rim regions (e.g. Venezky and Rutherford 1999; Coombs et al. 2000). Each of the magnetite–ilmenite pairs included in Table 3 pass the MgO/MnO criteria for equilibrium formulated by Bacon and Hirschmann (1988). The data from Table 3 is plotted in a curve of temperature versus fO_2 shown in Fig. 4. These data demonstrate that most of the core and rim temperature estimates fall between 871 and 900°C with most uncertainties near ± 20°C, and log fO_2 from – 11.1 to – 11.7, or 0.8 ± 0.2 log units above NNO (Andersen and Lindsley 1988). Three temperature estimates fall between 920 and 942°C, corresponding to two rim measurements and one average of three core analyses (P11a; Table 3). The P11a average data point falls off the trend produced by all other data, and thus is suspect. The compositions of those points indicate a subtle zonation in Ti towards the rims of the ilmenite grains in those pairs, though the errors on the average core and rim points tend to be large. This zonation could signify heating of the rhyodacite, presumably by the co-erupted andesite, prior to or during the eruption.

Use of the QUILF program (Andersen et al. 1993) to predict pre-eruptive temperatures from the co-existing pyroxenes in the rhyodacite yielded estimates of 948–1,026°C, with uncertainties of ± 68–153°C. The data used in QUILF consists of individual microprobe data points from each of the grains analyzed, which were used to formulate the averages given in Table 2. The QUILF model is useful in examining equilibrium between the co-existing pyroxenes, and the large uncertainties indicate that the rhyodacite augite and hypersthene pyroxenes are not in equilibrium. A further test involved fixing the composition of one pyroxene at a time, and letting the QUILF program fit for the other pyroxene's composition while estimating the temperature. In most cases, the two independently estimated temperatures did not agree within 25°C, nor did the composition of the variable pyroxene fit by QUILF agree with the microprobe analyses. Thus, use of the two pyroxene geothermometer is not reliable, and indicates that the scarce augite is indeed xenocrystic.

Constraints on pre-eruptive temperatures and fO_2 from the CFE andesite are problematic, since neither Fe–Ti oxides nor QUILF provide reliable estimates. Although Dreher et al. (2005) report temperatures from Fe–Ti oxide pairs of ~890 and ~1,100°C for the andesite, the lower temperature estimate was obtained from sample AC36b banded pumice and thus likely contains magnetite–ilmenite pairs from the rhyodacite. The higher temperature estimate exceeds the liquidus estimated using MELTS models (Ghiorso and Sack 1995; Asimow and Ghiorso 1998), as described below. Use of the QUILF (Andersen et al. 1993) two pyroxene geothermometer yielded temperatures between 947 and 1,012°C, with uncertainties greater than ± 100°C. This indicates that the pyroxenes in the andesite are not in equilibrium, and in this case, it is the hypersthene that is suspect as described above. The cpx-liquid thermobarometer of Putirka et al. (2003)

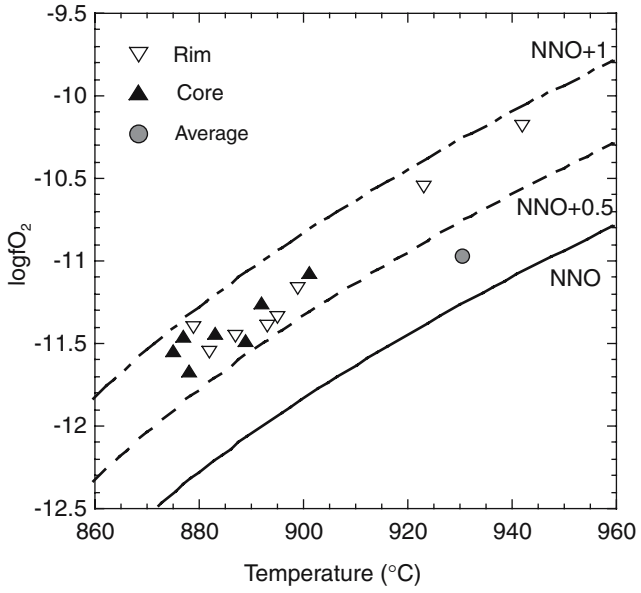

Fig. 4 This figure shows the temperature estimates derived from Fe–Ti oxide pair (magnetite–ilmenite) compositions, as determined using the models of Stormer (1983) and Andersen and Lindsley (1988). Temperatures plotted against fO_2 show that the temperature ranges and fO_2 used in the experiments agree well with those estimated for the natural magmas. Also notable are the rim temperatures that extend up to ~940°C, although the averaged data point in this temperature range falls off the trend and is suspect

does provide an estimate of 1,050–1,070°C based on the andesite augite and groundmass glass compositions (Tables 1, 2).

P_{H_2O} estimates from melt inclusions

The melt inclusions analyzed using FTIR contain 0.87 (± 0.04) to 3.06 (± 0.16) wt% total H_2O, with negligible CO_2 (Table 4). The VBD estimates from electron microprobe analyses of different melt inclusions yield an average estimate of 5.0 (± 0.6) wt% (electronic supplement). This estimate is derived by averaging the water contents that fall within 25% of the highest value obtained through analyses of different melt inclusions (~5.6 wt%; see supplemental data). The melt inclusion FTIR results predict entrapment pressures of ~65 MPa, while the higher H_2O contents estimated through the VBD method predict pressures of ~150 MPa. It is possible that the VBD estimates are skewed towards higher H_2O contents if Na migration problems are not adequately corrected. On the other hand, the melt inclusions analyzed using FTIR could give lower total H_2O because of leaking through cracks and capillaries in the plagioclase host crystals.

The melt inclusions from magnetite phenocrysts in the andesite provide a first approximation of the pre-eruptive pressure estimates, and were selected over the plagioclases because those tend to have rhyodacitic inclusion glass compositions and are suspected of originating within the rhyodacite (Fig. 2). Although the volatiles VBD method is not as accurate as FTIR, the opacity of the oxides would make double polishing the melt inclusions for spectroscopy extremely difficult. Inclusion water contents range from 0.4 to 4.1 wt% (Electronic supplement), with the average of the top 25% of the population yielding 3.5 (±0.5) wt%. Using the bulk composition of the andesite and the solubility model of Moore et al. (1998), this corresponds to entrapment pressures of ~110 MPa at 1,000°C. One drawback of the VBD estimate is that it cannot provide information on CO_2 contents in the inclusions. Entrapment pressure estimates based on H_2O alone, with no information on CO_2 contents, should be viewed as minima (e.g., Wallace 2005).

Rhyodacite experimental results

Most experimental run products consist of a combination of glass, Fe–Ti oxides, plagioclase, hypersthene, augite, and amphibole in varying proportions depending on the experimental conditions (Table 5, Fig. 5). At 950°C the quenched run consists entirely of glass. Oxides, predominantly magnetite, exist in all subliquidus runs. Apatite crystallizes at the lowest P_{H_2O} and T of all phases shown in the phase diagram. The phase assemblage thought to be stable in the natural rhyodacite, oxides, plagioclase, hypersthene, and

Table 4 Melt inclusion water contents from FTIR analyses

Incl.[a]	Thickness (μm)	Wt% H_2O (5,200 cm^{-1})[b]	Wt% OH (4,500 cm^{-1})[b]	Total H_2O (wt%) FTIR
f	29 (1)	1.71	0.86	2.57 (08)
3	19 (1)	2.13	0.92	3.05 (16)
h	39(1)	1.78	1.00	2.78 (07)
b	24 (10)	1.48	0.73	2.21 (92)
c mi1	37 (3)	1.87	0.95	2.82 (23)
c mi5	32 (2)	1.41	0.75	2.16 (14)
d mi1	41 (2)	0.82	0.50	0.87 (04)
c mi2	37 (3)	1.87	0.95	2.82 (23)
d mi2	41 (2)	1.00	0.62	1.62 (08)

[a]Incl. refers to the specific inclusion sample number. All inclusions analyzed using FTIR came from sample location 98ACJL1b

[b]ε values are 1.5 and 1.85 l mol^{-1} cm^{-1} calibrated for rhyolite glasses by Ihinger et al. (1994). The numbers in brackets are the uncertainties in thicknesses and water contents, derived from the thickness errors

amphibole, crystallizes over a wide range of P and T (Table 5, Fig. 5).

Experimental plagioclase compositions change predominantly with P_{H_2O} (e.g. Housh and Luhr 1991). The dotted curves in Fig. 5 outline the range of experimental plagioclase compositions as a function of experimental P_{H_2O} and T, which vary between An_{33-35} at P_{H_2O} ~80 MPa and An_{38-39} at P_{H_2O} > 125 MPa. However, the compositions also become more calcic as temperature increases above ~870°C, indicating that the compositions are also temperature dependent near the plagioclase mineral-in curve.

Hypersthene crystallized with compositions between $Wo_5En_{58}F_{36}$ and $Wo_2En_{66}Fs_{31}$ (Table 6), all similar to those from the natural rhyodacite. Calcium-rich augite crystallized in some of the experiments, with compositions ranging between $Wo_{35}En_{44}Fs_{21}$ and $Wo_{43}En_{35}Fs_{20}$. Of those analyzed, the closest in agreement with augite found in the natural rhyodacite crystallized in experiment ACP8, equilibrated at 130 MPa and 840°C, or about 40°C cooler than the Fe–Ti oxide estimates of the pre-eruptive temperatures. However, this experiment is suspected of Ni infiltration artificially stabilizing the augite. Edenite and pargasite amphiboles crystallized in experiments run at P_{H_2O} > 95 MPa with RACP4 run at 130 MPa and 880°C most closely reproducing those from the natural pumices. Augite and amphibole coexist over a similar temperature range above ~95 MPa, except in ACP9, which was held for shorter than ~100 h (Hammer and Rutherford 2002; Larsen 2005) and thus may not have fully equilibrated.

Experimental glass compositions are presented in Table 6, normalized to 100% for comparison with the essentially dry natural groundmass glass. Figure 6 shows decreasing SiO_2 and K_2O, and increasing Al_2O_3 and CaO as a function of pressure to 150 MPa at 870–880°C. The shaded regions in Fig. 5 also outline where the experimental glass compositions intersect those of the groundmass glass from the natural pumice, providing an estimate of the pressure at which the magma last crystallized. SiO_2 in experimental glasses

Table 5 Experimental run conditions and phases crystallized

Run	Pressure (MPa)	Temperature (°C)	Duration (h)	Phase assemblage[a]
Rhyodacite[b]				
ACP1	65	880	120	gl, ox, pl, opx
ACP2	95	880	164	gl, ox, pl, opx, amph
ACP3	95	840	193	gl, ox, pl, opx, cpx,
ACP4	80	820	336	gl, ox, pl, opx, cpx
ACP5	110	870	144	gl, ox, pl, opx, cpx, amph
ACP6	90	890	74	gl, ox, pl, opx, cpx,
ACP7	110	840	175	gl, ox, pl, opx, amph
ACP8	130	840	144	gl, ox, pl, opx, cpx, amph
ACP9	120	870	72	gl, ox, pl, opx, amph
ACP10	130	840	217.5	gl, ox, pl, opx, amph
ACP11	150	870	168	gl, ox, pl, cpx, amph
ACP12	150	820	168	gl, ox, pl, opx, amph
ACP13	170	850	168	gl, ox, pl, opx, amph
ACP14	100	890	192	gl, ox, pl, opx, amph
ACP15	200	850	122	gl, ox, pl, opx, amph
ACP16	50	900	166	gl, ox, pl, opx
ACP17	150	890	96	gl, ox, amph
ACP18	150	950	15	gl
ACP20	120	925	13	gl
RACP4 (11, 16)[c]	130	880	96	gl, ox, opx, amph
RACP5 (13, 17)	170	865	100	gl, ox, pl, opx, amph
RACP6 (12, 14)	75	840	168	gl, ox, pl, opx, cpx, apt
RACP7 (7, 14)	100	860	120	gl, ox, pl, opx, cpx, amph
RACP8 (11, 18)	150	900	14	gl, ox, pl, amph
RACP9 (11, 18)	130	880	456	gl, ox, pl, opx, cpx, amph

[a]Phases crystallized are labeled as follows: *gl* glass, *ox* oxides, *pl* plagioclase, *opx* enstatite, *cpx* augite, *amph* amphibole, *apt* apatite

[b]Starting materials for all experiments, except the reversals, are powdered natural pumice from the Plinian fall section of the eruption. The pumice is crystal-poor and was not homogenized by melting prior to the runs

[c]Reversal experiments were run to check the stability of phases in certain places to help better constrain the phase stability curves. The reversals comprise both crystal and glass-rich starting materials from prior experimental runs, as noted in parentheses. For example, RACP4 (11, 16) is a reversal conducted using ACP11 and ACP16 run products as starting materials

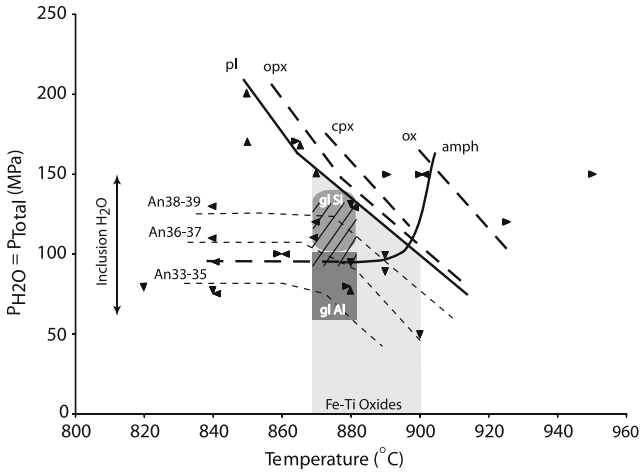

Fig. 5 Phase diagram for the Aniakchak CFE rhyodacite under H_2O-saturated conditions. Experimental runs are shown using *triangles* and their directions point towards the approach to equilibrium (Table 5). *Two triangles* meeting at one point denote a reversal experiment, run using starting materials from prior crystal and glass-rich experiments (Table 5). The phase-in curves for plagioclase (pl), hypersthene (opx), augite (cpx), amphibole (amph), and oxides (ox) are shown using *solid lines* where better constrained, and *dashed lines* where more uncertain. All curves, except for amphibole, are approximated using straight lines primarily because of a lack of resolution on their precise curvature as a function of P and T. The *shaded regions* outline the P–T regions where the natural phase compositions and modeled oxide temperatures compare well with those reproduced experimentally. The *vertical, light gray region* (Fe–Ti oxides), covers the temperature range predicted by oxide thermometry. The *dark gray vertical regions* (glSi and glAl) outline the P_{H_2O}-T regions where the experimental glass SiO_2 and Al_2O_3 compositions agree with those in the natural groundmass. The *hatched region* outlines the 95–130 MPa P_{total} range at 870–880°C predicted by the H_2O-undersaturated MELTS models for Al_2O_3, in comparison with the natural groundmass glass composition. The *short dashed curves* approximate how the experimental plagioclase compositions change as a function of P_{H_2O} and T

produced at 110–140 MPa and 870–880°C cross the field outlining the natural glass composition (Figs. 5, 6). H_2O-saturated experimental glass Al_2O_3 crosses the natural glass field between 65 and 110 MPa (Figs. 5, 6). Within this pressure range, Al_2O_3 values are ~0.8 wt% higher than in the natural glass. K_2O and CaO meet the natural glass composition at pressures >110 MPa. The divergence of the H_2O-saturated experimental glass Al_2O_3 from the natural groundmass relative to SiO_2 over a similar pressure range may indicate H_2O undersaturation in the natural magma (e.g., Hammer et al. 2002).

The two curves shown in Fig. 6 represent the predicted liquid line of descent of the melt using MELTS (Ghiorso and Sack 1995; Asimow and Ghiorso 1998). Both models ran for varying pressures at 880°C, with fO_2 equaling NNO, with one assuming H_2O saturation, and the other with $X_{H_2O} = 0.8$. The trends in SiO_2 and K_2O measured in the H_2O-saturated experimental glasses tend to follow those predicted by the H_2O-saturated MELTS models fairly well, with the H_2O-saturated experiments and model shifted to higher Al_2O_3 contents relative to the H_2O-undersaturated model. The H_2O-undersaturated MELTS curve predicts Al_2O_3 should intersect the natural groundmass glass at P_{total} between ~90 and 130 MPa, in better agreement with the pressure range predicted by the H_2O-saturated SiO_2 experimental trend (Figs. 5, 6). SiO_2 estimated from the H_2O-undersaturated MELTS model intersects the natural glass within a slightly higher, but narrower P_{total} range of ~125–150. CaO from the H_2O-undersaturated model is slightly but consistently ~0.1 wt% lower than the H_2O-saturated model, which intersects the natural glass >110 MPa. Incompatible K_2O does not change much between the two models.

Discussion

Pre-eruptive magma storage and movement

Figure 5 shows different shaded regions corresponding to pre-eruptive P and T estimates derived from different sources of data. The vertical shaded region outlines the 871–900°C Fe–Ti oxide derived temperature range, and the vertical arrow shows the ~65–150 P_{H_2O} range indicated by melt inclusion analyses. The two dark shaded regions labeled glSi and glAl denote the P_{H_2O} ranges over which H_2O-saturated experiments run at 870–880°C reproduce the natural groundmass compositions. The hatched region between 95 and 130 MPa denotes where Al_2O_3 predicted by the H_2O-undersaturated MELTS models reproduces the natural groundmass glass within the 870–880°C temperature range. Experimental plagioclase, shown by the dotted curves, compares well with the average An_{39} composition from the natural plagioclase between 75 and 150 MPa and 870 and 895°C. Experimental amphibole matches that in the natural pumice most closely at 130 MPa and 880°C. Assuming water saturation, the experimental and petrological data indicate that the rhyodacite magma equilibrated at P_{H_2O} between 110 and 140 MPa, and 870 and 895°C. Those pressures correspond to 4.2–5.3 km depth, assuming a lithostatic pressure gradient and crustal density of 2,700 kg m^{-3}. Seismic velocity studies reveal that the bulk of the upper, continental crust of the Alaska Peninsula is probably andesitic (e.g., Fliedner and Klemperer 2000) and the crustal density chosen for

Table 6 Experimental glass compositions

Run no. phase[a]	SiO_2	TiO_2	Al_2O_3	FeO_t	MnO	MgO	CaO	Na_2O	K_2O	F	Cl	Total[b]	Mol%
ACP1													
gl (3)	73.8(8)	0.33 (20)	14.3 (5)	1.60 (16)	0.12 (05)	0.23 (04)	1.58 (27)	5.44 (21)	3.35 (18)	0.11 (02)		96.00	
pl (1)	59.3		25.2	0.37			6.86	7.36	0.38			99.07	33
opx (3)	52.1 (1.0)	0.21 (11)	1.0 (4)	18.54 (98)	1.59 (39)	23.10 (71)	1.75 (35)					98.57	4–65–32
ACP2													
gl (6)	72.7 (3)	0.22 (10)	14.73 (29)	1.70 (10)	0.14 (04)	0.28 (03)	1.58 (13)	5.42 (20)	3.26 (15)	0.14 (05)		95.50	
opx (3)	52.7 (6)	0.24 (21)	0.99 (14)	19.35 (75)	1.87 (23)	22.55 (24)	1.48 (28)					99.28	3–63–33
amph (3)	43.5 (1.5)	2.98 (40)	9.7 (1.5)	14.24 (83)	0.66 (27)	12.68 (36)	9.83 (86)	2.39 (07)	0.49 (05)	0.20 (20)	0.09 (03)	96.81	
ACP3													
gl (2)	72.6 (8)	0.26 (10)	14.9 (5)	1.30 (13)	0.10 (07)	0.22 (08)	1.84 (24)	5.65 (31)	3.12 (22)	0.11 (02)		95.68	
pl (4)	59.3 (8)		25.4 (5)	0.48 (05)			6.98 (70)	7.41 (23)	0.42 (07)			99.95	34
cpx (1)	51.6	0.47	1.6	11.59	1.27	14.82	16.32	0.34				98.00	35–44–21
opx (2)	54.8 (9)	0.25 (08)	1.8 (1.1)	21.16 (1.39)	1.99 (03)	19.51 (4.4)	1.75 (62)					101.56	4–57–39
ACP4													
opx (2)	54.7 (1.7)	0.32 (10)	1.64 (99)	18.85 (65)	2.21 (02)	20.89 (2.51)	1.48 (17)					100.41	3–61–35
ACP5													
gl (2)	72.2 (3)	0.30 (08)	14.8 (1)	2.60 (17)	0.13 (05)	0.29 (07)	1.53 (06)	4.81 (10)	3.39 (14)	0.13 (02)		94.23	
opx (3)	52.2 (8)	0.25 (12)	0.8 (2)	18.67 (15)	1.47 (49)	22.00 (29)	1.27 (17)					96.83	3–64–33
ACP7													
gl (4)	71.8 (2)	0.26 (06)	14.7 (4)	1.48 (20)		0.30 (11)	1.65 (17)	6.15 (07)	3.12 (10)	0.15 (09)		95.87	
pl (3)	59.1 (1.0)		26.8 (2)	0.51 (04)			7.67 (30)	6.67 (16)	0.34 (02)			101.15	38
opx (4)	52.3 (5)	0.31 (09)	1.2 (6)	18.40 (2.17)	1.55 (33)	23.13 (1.51)	1.57 (17)					99.57	3–65–32
ACP8													
pl (5)	58.0 (7)		26.4 (9)	0.56 (11)			7.82 (70)	6.62 (34)	0.35 (05)			99.78	38
cpx (3)	52.5 (1.1)	0.39 (36)	1.7 (1.2)	9.95 (1.06)	0.71 (52)	14.63 (1.07)	18.98 (1.41)	0.38 (03)				99.36	39–42–17
amph (1)	43.5	3.38	10.5	11.79	0.51	13.97	10.18	2.64	0.43	0.31	0.06	97.32	
ACP9													
gl (2)	71.9 (1)	0.46 (24)	15.0 (1)	1.87 (14)	0.13 (08)	0.33 (04)	1.76 (07)	5.56 (24)	3.15 (13)	0.17 (02)		95.11	
pl (4)	59.7 (2)		25.8 (2)	0.55 (13)			7.17 (27)	6.95 (13)	0.40 (02)			100.57	36
opx (2)	52.8 (1.0)	0.19 (07)	0.7 (6)	19.29 (84)	1.85 (05)	21.99 (1.29)	1.41 (10)	–	–			98.33	3–63–34
amph (1)	46.5	2.72	10.3	11.67	0.67	10.97	9.7	2.23	0.63		0.03	95.42	
ACP10													
pl (3)	58.7 (5)		25.3 (6)	0.38 (08)			7.68 (42)	7.34 (17)	0.31 (04)			99.63	36
opx (1)	54.2	0.18	0.4	17.95	2.43	24.35	1.1	–	–			101.12	2–66–31
ACP11													
gl (4)	70.6 (6)	0.33 (21)	15.7 (2)	2.36 (31)	–	0.35 (02)	1.89 (04)	5.50 (27)	2.91 (08)	0.06 (01)		94.84	
pl (1)	58.3		26.4	0.51			7.63	6.47	0.38			99.72	39
cpx (3)	52.0 (7)	0.49 (03)	1.9 (6)	12.16 (2.21)	1.07 (14)	13.92 (1.85)	15.75 (2.59)	0.46 (16)	–			97.82	35–43–23
ACP13													
pl (4)	58.4 (3)		27.0 (3)	0.29 (14)			8.21 (22)	6.56 (28)	0.29 (04)			100.7	39
ACP14													
gl (1)	71.7	0.37	14.3	2.31	–	0.3	1.67	6.44	3.04	0.08		95.51	
pl (5)	58.1 (8)		26.4 (4)	0.41 (07)			7.79 (32)	6.75 (18)	0.32 (06)			99.78	38
opx (3)	53.7 (3)	0.24 (07)	0.9 (4)	19.56 (62)	1.69 (13)	21.44 (2.02)	1.50 (31)	–	–			99.2	3–62–35

Table 6 continued

Run no. phase[a]	SiO_2	TiO_2	Al_2O_3	FeO_t	MnO	MgO	CaO	Na_2O	K_2O	F	Cl	Total[b]	Mol%
ACP15													
gl (2)	70.2 (2)	0.49 (01)	15.4 (2)	2.10 (28)	–	0.33 (03)	2.23 (16)	6.26 (01)	2.94 (27)	0.25 (16)		94.33	
pl (1)	57.0		26.8	0.51			8.06	6.72	0.51			99.4	38
amph (3)	46.3 (9)	1.93 (54)	8.7 (5)	14.19 (88)	0.68 (12)	13.44 (56)	9.91 (32)	2.25 (14)	0.45 (07)	0.42 (41)	0.07 (05)	98.32	
ACP16													
gl (3)	70.7 (3)	0.57 (29)	14.5 (5)	2.62 (55)	–	0.40 (26)	1.91 (16)	6.27 (08)	3.11 (13)	0.22 (03)		94.74	
pl (1)	57.9		26.1	0.6			7.82	6.89	0.36			99.71	37
opx (1)	52.8	0.29	0.9	18.59	1.57	22.70	1.79	–	–			98.89	3–64–32
ACP18													
gl (13)	70.4 (5)	0.57 (04)	14.7 (2)	2.59 (20)	–	0.58 (04)	2.10 (06)	5.82 (37)	3.21 (07)	0.22 (05)		93.95	
ACP20													
gl (8)	71.14 (75)	0.66 (30)	15.0 (2)	2.76 (17)		0.56 (03)	1.90 (06)	4.20 (18)	2.72 (12)	0.17 (04)		96.11	
R4ACP11													
gl (6)	71.0 (6)	0.64 (19)	15.9 (2)	1.87 (21)		0.46 (03)	1.85 (03)	5.49 (39)	2.96 (11)	0.09 (02)		95.48	
amph (2)	42.1 (2)	3.81 (16)	11.0 (2)	12.17 (20)	0.42 (09)	13.42 (05)	10.34 (13)	2.58 (05)	0.39 (02)	0.35 (35)	0.03 (03)	96.65	
R4ACP16													
gl (1)	71.5	0.48	15.6	1.74		0.52	1.83	5.76	2.80	0.01		95.34	
opx (2)	52.4 (0)	0.30 (01)	0.6 (0)	18.57 (43)	1.69 (08)	23.17 (21)	1.46 (28)					98.24	3–65–32
R5ACP13													
gl (9)	72.8 (2)	0.30 (08)	15.6 (1)	2.04 (13)		0.32 (03)	1.93 (08)	3.82 (16)	2.42 (09)	0.10 (02)		94.59	
R5ACP17													
gl (20)	72.3 (4)	0.34 (11)	15.8 (1)	2.29 (54)		0.37 (03)	1.93 (09)	3.84 (12)	2.39 (09)	0.06 (02)		94.03	
R6ACP12													
gl (2)	76.1 (4)	0.72 (23)	13.5 (2)	1.00 (06)		0.10 (01)	0.80 (20)	3.84 (19)	3.58 (12)	0.02 (01)		95.62	
pl (4)	59.7 (1.0)		25.6 (1.0)	0.75 (35)			6.56 (79)	7.52 (36)	0.49 (14)			100.84	31
R6ACP16													
gl (3)	76.8 (1.0)	0.17 (10)	13.5 (3)	1.14 (09)		0.12 (01)	0.47 (03)	3.64 (16)	3.32 (17)	0.04 (03)		96.35	
pl (4)	59.5 (7)		25.3 (4)	0.68 (40)			6.17 (14)	7.75 (18)	0.46 (05)			100.37	30
R7ACP14													
gl (3)	74.8 (9)	0.42 (04)	15.2 (2)	0.92 (12)		0.28 (05)	1.31 (05)	3.87(20)	3.30 (04)	0.10 (03)		95.84	
pl (6)	58.1 (1.0)		26.6 (6)	0.45 (07)			7.58 (65)	7.09 (31)	0.34 (04)			100.30	36
R9ACP11													
gl (1)	71.7	0.37	15.5	1.52		0.27	1.33	6.06	3.24			92.43	
cpx (4)	50.8 (1.0)	0.46 (28)	1.2 (5)	11.59 (35)	1.32 (39)	12.28 (49)	21.27 (46)	0.37 (10)				99.58	43–35–20
R9ACP18													
gl (1)	71.7	0.25	15.2	1.73		0.34	1.58	5.78	3.11			91.68	
amph (3)	45.1 (4)	2.27 (29)	8.3 (5)	13.70 (21)	1.00 (43)	14.14 (16)	9.02 (11)	2.14 (07)	0.29 (01)	0.29 (29)	0.07 (02)	96.40	

[a]Run/phase: The subheadings for each starting row of data denote the experimental run numbers. Beneath each phase is listed as follows: *gl* glass, *pl* plagioclase, *opx* hypersthene, *cpx* augite, *amph* amphibole

[b]All glass analyses are reported normalized to 100%, with the unnormalized totals reported

this study allows a direct comparison with studies on other Aleutian and Kamchatkan arc volcanic eruptions (Coombs and Gardner 2001; Hammer et al. 2002; Izbekov et al. 2004).

The assumption of water saturation for the Aniakchak rhyodacite magma may not be correct, however. The mismatch in the P_{H_2O} predicted by experimental SiO_2, Al_2O_3, and CaO compositions in comparison with the natural glasses is suspect. Hammer et al. (2002) performed a series of H_2O-saturated and H_2O-undersaturated experiments on the andesite and dacite erupted in 1912 from Novarupta in the Valley of Ten Thousand Smokes, Alaska. Those experiments show Al_2O_3 in H_2O-saturated experiments (72 wt% SiO_2) differ by ~0.8 wt% relative to H_2O-undersaturated runs at the same temperature, driven by changes in crystallization of plagioclase. It is interesting to note that Al_2O_3 in the Aniakchak H_2O-saturated experiments is ~0.8 wt% higher relative to the pressure range predicted from the experimental glass SiO_2. The MELTS H_2O-undersaturated runs, however, do predict a trend in Al_2O_3 that intersects the natural groundmass data over a P_{total} range of ~90–130 MPa. This estimate is consistent with the pressure range indicated primarily by SiO_2 from the H_2O-saturated experiments. The slight shift in the P_{total} range predicted from the H_2O-undersaturated SiO_2 trend does make the comparison worse, though they do overlap between 125 and 130 MPa. The shift in CaO predicted by the H_2O-undersaturated models is within error of most of the experimental data points, but the agreement with the natural groundmass glass is not as good. Although the MELTS H_2O-undersaturated model also has inconsistencies between the different oxides (Fig. 6), the model results fit the natural glass compositions more consistently than either the H_2O-saturated experiments or models. This indicates that the Aniakchak rhyodacite magma was probably water undersaturated, and elevates the predicted storage pressure range to between 125 and 150 MPa P_{total} (4.5 and 5.4 km).

Andesite constraints

The andesite proved problematic in using phase equilibria experiments to constrain pre-eruptive storage conditions. Its disequilibrium phenocryst assemblage makes application of the experimental and geothermometry methods difficult. Its crystal-poor nature makes it difficult to converge on a unique solution of pre-eruptive magma P and T through a comparison between experimental and natural glass compositions. In this case, the MELTS model provides a relatively inexpensive and less time-consuming way to approximate the temperatures and pressures at which the mineral phases in the andesite probably grew, through comparing the groundmass glass compositions with the liquid line of descent predicted by the model. Aleutian arc basalt and andesite liquid lines of descent are reproduced reasonably with fO_2 of NNO to NNO + 2 log units (e.g., Baker and Eggler 1983; Sisson and Grove 1993). A rough estimate of the pre-eruptive temperature was made using MELTS, starting with the bulk composition, a liquidus temperature calculated of ~1,050°C, and letting it crystallize under equilibrium

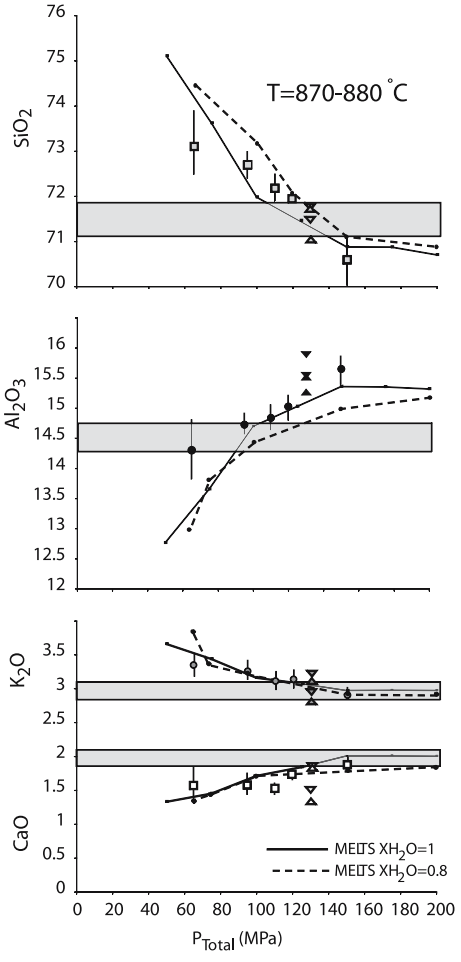

Fig. 6 Rhyodacite experimental glass compositions plotted versus P_{H_2O} at 870–880°C. The *circles and squares* represent melting and crystallization experiments, undifferentiated: *white squares*, CaO; *gray circles*, K_2O; *black circles*, Al_2O_3; and *gray squares*, SiO_2. The *regular and inverted triangles* denote reversal experiments. The *shaded regions* denote the composition of the natural groundmass glass, and their widths represent 1σ about the average glass composition. The *solid lines* show the predicted liquid line of descent as a function of pressure as modeled in MELTS at fO_2 = NNO, T=880°C and H_2O-saturated conditions. The *dashed curves* represent the MELTS liquid line of descent for X_{H_2O} = 0.8 and similar P_{total} and T

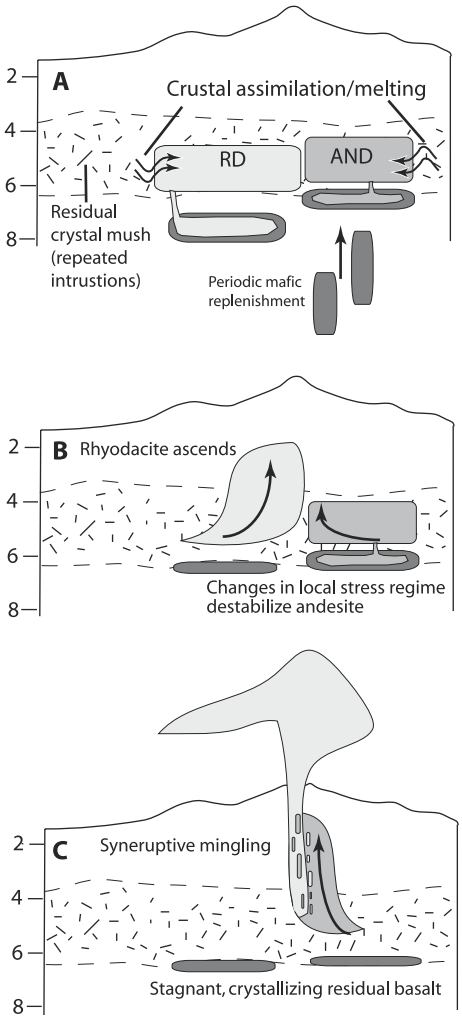

Fig. 7 This cartoon illustrates a model for pre-eruptive magma storage and ascent prior to the caldera-forming eruption. The *rectangular regions* show the inferred storage depths of the rhyodacite (RD) and andesite (AND). These cartoons are illustrative only and are not meant as an exact replica of the sub-surface plumbing system. **a** RD and AND CFE magmas were stored at similar depths of 4.5–5.4 and > 4.1 km, respectively, within the crust. It is likely that those magmas originated in the same or chemically similar mush zones (stipled pattern), and were affected differently by crustal assimilation and magma mixing processes (e.g., George et al. 2004; Dreher et al. 2005). **b** The rhyodacite may have ascended, which could have destabilized the andesite nearby triggering its ascent shortly after. **c** Pervasive syn-eruptive mingling probably occurred within the conduit, resulting in crystal exchange (e.g., Fig. 3) and μm to cm scale banding observed within all stratigraphic levels

conditions and fO_2 equal to NNO. The liquid line of descent predicted by MELTS converges on that of the natural groundmass glass at a temperature of ~1,000°C under H_2O-saturated conditions and a wide range of pressures (50–150 MPa). This estimate is ~60°C cooler than predicted by the cpx-liquid geothermobarometer of Putirka et al. (2003), using the augite and bulk rock compositions provided in Tables 1 and 2, indicating augite formed on the liquidus.

Combined with the MELTS temperature constraints, the melt inclusion VBD data from electron microprobe analyses indicates approximate storage pressures of 110 MPa, corresponding to a depth of ~4.1 km. Those estimates assume the andesite was H_2O saturated, yet no constraints on P_{CO_2} exist. If the andesite was H_2O undersaturated, the melt inclusion pressure/depth estimates must be viewed as minima since they are based on assuming $P_{total} = P_{H_2O}$. This result offers a very general constraint on the storage conditions of the andesite, indicating that the two magmas may have originally been stored at similar depths prior to the eruption, or the rhyodacite was stored slightly deeper if the andesite was H_2O saturated.

Implications for the 3430 yBP Aniakchak caldera-forming eruption

The preferred model to explain the phase equilibria results, consistent with the prior geochemical studies (George et al. 2004; Dreher et al. 2005), starts with storage of two separate magma bodies at similar depths of ~4.1–5.5 km (Fig. 7), though the depth estimates, particularly for the andesite, are minima. Although it is tempting to place the magmas within the same, stratified magma chamber, the prior geochemical studies (George et al. 2004; Dreher et al. 2005) indicate that they are not directly related through fractionation of magma parental to the andesite. Both CFE magmas probably evolved within an extensive mush column, built up through time by repeated replenishment of the system from deeper sources. Despite similar residence depths, they may not have been in physical contact initially, causing differences in their AFC dominated geochemical signatures (e.g., Brophy and Dreher 2000; George et al. 2004; Dreher et al. 2005). They also could have been extracted as liquids from separate, but spatially adjacent crystallizing magma batches over a relatively short amount of time before ascent (e.g., Sisson and Bacon 1999). Brophy and Dreher (2000) discuss a similar model for the generation of compositional gaps such as that seen at Aniakchak (Fig. 2) through magma mixing and fractionation processes at South Sister volcano, Oregon. There, the magmas are hypothesized to have originated as multiple, discrete, and separately evolving bodies of basalt, andesite, and rhyolite at any given time. This can lead to magmas that have some geochemical evidence for being related, yet are overprinted by magma mixing and assimilation signatures.

The Aniakchak eruption probably started with ascent of the rhyodacite, triggered either by a large change in the regional tectonic stress field through an earthquake, or overpressure in the magma chamber leading to sufficient opening of fractures to allow for the passage of the magma. If the two magmas resided in close proximity, ascent of ~10 km^3 magma should also have changed the local stress field around the andesite reservoir (e.g., Takada 1989; Gudmundsson 1998), essentially dragging it up along with the rhyodacite. Conversely, it is possible that the andesite magma started to ascend first, intersecting the shallower rhyodacite magma and triggering the eruption. This sequence would better explain the somewhat ephemeral evidence for zonation in the ilmenite used for thermometry estimates, predicting heating of the rhyodacite up to ~942°C (Fig. 4). If the andesite ascended nearly simultaneously along the same conduit, syn-eruptive mingling would result. An analogous situation may have existed beneath Katmai and Novarupta prior to the 1912 eruption (Coombs and Gardner 2001; Hammer et al. 2002). In that case, the magmas erupted from the same vent, and laterally separate storage regions at similar depths are invoked to help explain the simultaneous collapse of Katmai caldera 10 km away from Novarupta.

Conclusions

Petrologic and experimental data from the Aniakchak CFE rhyodacite and andesite eruption products yield constraints on pre-eruptive magma storage and dynamics. Fe–Ti oxide thermometry results yield pre-eruptive temperature and fO_2 estimates for the rhyodacite of 871–900°C and fO_2 of NNO + 0.5 to 1 log units. H_2O-saturated phase equilibria experiments replicate the phenocryst populations and compositions of the rhyodacite in a P–T range from 95 to 150 at 870–880°C. Experimental glass data reveal a mismatch between SiO_2 and Al_2O_3 in their agreement with the natural groundmass, with SiO_2 predicting P_{H_2O} between 110 and 140 MPa and Al_2O_3 predicting 65–110 MPa. MELTS models (Ghiorso and Sack 1995; Asimow and Ghiorso 1998) run for water-undersaturated conditions alleviate the mismatch between SiO_2 and Al_2O_3 to some degree. The range in P_{total} between 125 and 150 MPa predicted from a comparison between the undersaturated liquid line of descent and the natural glass compositions is slightly higher than from the H_2O-saturated experiments, and correspond to storage at 4.5–5.4 km depth in the crust. The nearly aphyric nature of the andesite points to a near-liquidus pre-eruptive temperature, estimated at ~1,000°C using MELTS. Volatiles by difference data from melt inclusions in titanomagnetite from the andesite yield a minimum storage pressure of ~110 MPa, when P_{H_2O} is assumed to equal P_{total}. This corresponds to storage at a minimum depth of 4.1 km. The estimates indicate similar residence depths for both the rhyodacite and andesite CFE magmas prior to eruption. Ultimately, the CFE andesite and rhyodacite show evidence for origination in a common mush zone, yet were probably physically separated (George et al. 2004; Dreher et al. 2005), similar to Katmai/Novarupta prior to 1912 (Coombs and Gardner 2001; Hammer et al. 2002). Yet, they must have been close enough so that they ascended nearly simultaneously, which is necessary to explain the mingling which affects the eruption deposits on all levels and scales.

Acknowledgements This work was supported by the Alaska Volcano Observatory and National Science Foundation grant EAR 0106658. K. Severin provided assistance with the electron microprobe and J. Lowenstern provided the use of the Nicolet FTIR spectrometer at the USGS (Menlo Park). S. Dreher, J. Eichelberger, J. Gardner, and T. Neal contributed discussions, figures, and access to data that improved this work. The author thanks C. Bacon and M. Coombs for comments that improved the manuscript prior to submission. The author thanks J. Hammer and E. Cottrell for reviews that improved this study.

References

Andersen DJ, Lindsley DH (1988) Internally consistent solution models for Fe–Mg–Mn–Ti oxides; Fe–Ti oxides. Am Mineral 73:714–726

Andersen DJ, Lindsley DH, Davidson PM (1993) QUILF: a PASCAL program to assess equilibria among Fe–Mg–Ti oxides, pyroxenes, olivine, and quartz. Comput Geosci 19:1333–1350

Asimow PD, Ghiorso MS (1998) Algorithmic modifications extending MELTS to calculate subsolidus phase relations. Am Mineral 83:1127–1132

Bacon CR, Hirschmann MM (1988) Mg/Mn partitioning as a test for equilibrium between coexisting Fe–Ti oxides. Am Mineral 73:57–61

Baker DR, Eggler DH (1983) Fractionation paths of Atka (Aleutians) high-alumina basalts: constraints from phase relations. J Volcanol Geotherm Res 18:387–404

Begét JE, Mason OK, Andersen PM (1992) Age, extent and climatic significance of the c. 3400 BP Aniakchak tephra, western Alaska, USA. Holocene 2:51–56

Brophy JG, Dreher ST (2000) The origin of composition gaps at South Sister volcano, central Oregon: implications for fractional crystallization processes beneath active calc-alkaline volcanoes. J Volcanol Geotherm Res 102:287–307

Coombs ML, Gardner JE (2001) Shallow-storage conditions for the rhyolite of the 1912 eruption at Novarupta, Alaska. Geology 29:775–778

Coombs ML, Eichelberger JC, Rutherford MJ (2000) Magma storage and mixing conditions for the 1953–1974 eruptions of Southwest Trident volcano, Katmai National Park, Alaska. Contrib Mineral Petrol 140:99–118

Devine JD, Gardner JE, Brack HP, Layne GD, Rutherford MJ (1995) Comparison of microanalytical methods for estimating H_2O contents of silicic volcanic glasses. Am Mineral 80:319–328

Dreher ST (2002) The physical volcanology and petrology of the 3400 YBP caldera-forming eruption of Aniakchak Volcano, Alaska. Ph.D. thesis, University of Alaska Fairbanks, Fairbanks, AK, 174 pp

Dreher ST, Eichelberger JC, Larsen JF (2005) The petrology and geochemistry of the Aniakchak Caldera-forming ignimbrite, Aleutian arc, Alaska. J Petrol 46:1747–1768

Fliedner MM, Klemperer SL (2000) The transition from oceanic arc to continental arc in the crustal structure of the Aleutian Arc. Earth Planet Sci Lett 179:567–579

George R, Turner S, Hawkesworth C, Bacon CR, Nye CJ, Stelling P, Dreher S (2004) Chemical versus temporal controls on the evolution of tholeiitic and calc-alkaline magmas at two volcanoes in the Alaska–Aleutian arc. J Petrol 45:203–219

Ghiorso MS, Sack RO (1995) Chemical mass transfer in magmatic processes IV. A revised and internally consistent thermodynamic model for the interpolation and extrapolation of liquid–solid equilibria in magmatic systems at elevated temperatures and pressures. Contrib Mineral Petrol 119:197–212

Gudmundsson A (1998) Formation and development of normal-fault calderas and the initiation of large explosive eruptions. Bull Volcanol 60:160–170

Hammer JE, Rutherford MJ (2002) An experimental study of the kinetics of decompression-induced crystallization in silicic melt. J Geophys Res 107: DOI 10.1029/2001JB000281

Hammer JE, Rutherford MJ, Hildreth W (2002) Magma storage prior to the 1912 eruption at Novarupta, Alaska. Contrib Mineral Petrol 144:144–162

Housh TB, Luhr JF (1991) Plagioclase-melt equilibria in hydrous systems. Am Mineral 76:477–492

Ihinger PD, Hervig RL, Paul F, McMillan PF (1994) Analytical methods for volatiles in glasses. Rev Mineral 30:67–121

Izbekov PE, Eichelberger JC, Ivanov BV (2004) The 1996 eruption of Karymsky volcano, Kamchatka: historical record of basaltic replenishment of an andesite reservoir. J Petrol 45:2325–2345

Johnson DM, Hooper PR, Conrey RM (1999) XRF analysis of rocks and minerals for major and trace elements on a single low dilution Li-tetraborate fused bead. Adv X-ray Anal 41:843–867

Larsen JF (2005) Experimental study of plagioclase rim growth around anorthite seed crystals in rhyodacitic melt. Am Mineral 90:417–427

Miller TP, Smith RL (1977) Spectacular mobility of ash flows around Aniakchak and Fisher calderas, Alaska. Geology 5:173–176

Miller TP, Smith RL (1987) Late Quaternary caldera-forming eruptions in the eastern Aleutian arc, Alaska. Geology 15:434–438

Moore G, Vennemann T, Carmichael ISE (1998) An empirical model for the solubility of H_2O in magmas to 3 kilobars. Am Mineral 83:36–42

Neal CA, McGimsey RG, Miller TP, Riehle JR, Waythomas CF (2001) Preliminary volcano-hazard assessment for Aniakchak Volcano, Alaska. U.S. Geological Survey Open-File Report OF 00–0519, 35 pp

Putirka KD, Mikaelian H, Ryerson F, Shaw H (2003) New clinopyroxene-liquid thermobarometers for mafic, evolved, and volatile-bearing lava compositions, with applications to lavas from Tibet and the Snake River Plain, Idaho. Am Mineral 88:1542–1554

Sisson TW, Bacon CR (1999) Gas-drive filter pressing in magmas. Geology 27:613–616

Sisson TW, Grove TL (1993) Temperatures and H2O contents of low-MgO high-alumina basalts. Contrib Mineral Petrol 113:167–184

Stormer JC (1983) The effect of recalculation on estimates of temperature and oxygen fugacity from analysis multicomponent iron–titanium oxides. Am Mineral 68:586–594

Tait S (1992) Selective preservation of melt inclusions in igneous phenocrysts. Am Mineral 77:146–155

Takada A (1989) Magma transport and reservoir formation by a system of propagating cracks. Bull Volcanol 52:118–126

Venezky DY, Rutherford MJ (1999) Petrology and Fe–Ti oxide reequilibration of the 1991 Mount Unzen mixed magma. J Volcanol Geotherm Res 89:213–230

Wallace PJ (2005) Volatiles in subduction zone magmas: concentrations and fluxes based on melt inclusion and volcanic gas data. J Volcanol Geotherm Res 140:217–240

Waythomas CF, Neal CA (1998) Tsunami generation by pyroclastic flow during the 3500-year B.P. caldera-forming eruption of Aniakchak Volcano, Alaska. Bull Volcanol 60:110–124

Waythomas CF, Walder JS, McGimsey RG, Neal CA (1996) A catastrophic flood caused by drainage of a caldera lake at Aniakchak Volcano, Alaska, and implications for volcanic hazards assessment. GSA Bull 108:861–871